Measurement of rivulet movement and thickness on inclined cable using videogrammetry

Haiquan Jing[1a], Yong Xia[*1], Youlin Xu[1b] and Yongle Li[2c]

[1]*Department of Civil and Environmental Engineering, The Hong Kong Polytechnic University, Hong Kong*
[2]*Department of Bridge Engineering, Southwest Jiaotong University, Chengdu, China*

Abstract.   Stay cables in some cable-stayed bridges suffer large amplitude vibrations under the simultaneous occurrence of rain and wind. This phenomenon is called rain–wind-induced vibration (RWIV). The upper rivulet oscillating circumferentially on the inclined cable surface plays an important role in this phenomenon. However, its small size and high sensitivity to wind flow make measuring rivulet size and its movement challenging. Moreover, the distribution of the rivulet along the entire cable has not been measured. This paper applies the videogrammetric technique to measure the movement and geometry dimension of the upper rivulet along the entire cable during RWIV. A cable model is tested in an open-jet wind tunnel with artificial rain. RWIV is successfully reproduced. Only one digital video camera is employed and installed on the cable during the experiment. The camera records video clips of the upper rivulet and cable movements. The video clips are then transferred into a series of images, from which the positions of the cable and the upper rivulet at each time instant are identified by image processing. The thickness of the upper rivulet is also estimated. The oscillation amplitude, equilibrium position, and dominant frequency of the rivulet are presented. The relationship between cable and rivulet variations is also investigated. Results demonstrate that this non-contact, non-intrusive measurement method has good resolution and is cost effective.

Keywords: cable vibration; rain–wind-induced vibration; rivulet movement; rivulet thickness; image processing

1. Introduction

Stay cables are prone to large vibrations excited by external excitation (e.g., wind, rain, vehicles, and anchor motions) because of their inherent low damping and high flexibility characteristics (Xia and Fujino 2006). Large cable vibrations have been observed in the stay cables of several cable-stayed bridges under the simultaneous occurrence of rain and wind (Ohshima and Nanjo 1987, Hikami and Shiraishi 1988, Matsumoto *et al.* 1989, Saito *et al.* 1994, Ni *et al.* 2007). This phenomenon is called rain–wind-induced vibration (RWIV).

∗Corresponding author, Associate Professor, E-mail: ceyxia@polyu.edu.hk
[a] Ph.D. Student, Email: 12900160r@connect.polyu.hk
[b] Professor, Email: ceylxu@polyu.edu.hk
[c] Professor, Email: lele@swjtu.edu.cn

Extensive research has been conducted through field measurement (Main and Jones 1999, Ni *et al.* 2007, Zuo *et al.* 2008), wind tunnel test (Hikami and Shiraishi 1988, Matsumoto *et al.* 1992, 1995, 2003, Gu and Du 2005, Li *et al.* 2010b), and theoretical analysis (Wang and Xu 2003, Xu and Wang 2003, Wilde and Witkowski 2003, Seidel and Dinkler 2006) to investigate RWIV. Many researchers believe that the upper rivulet plays an important role in RWIV. Accurate rivulet information improves the revelation of the excitation mechanisms of RWIV.

Lemaitre *et al.* (2007, 2010) proposed a lubrication theory-based numerical model to simulate the evolution of a water film around a cylinder under gravity and wind load, which was measured from the static dry cylinder. They predicted the rivulets' location and wind speed range for the rivulets' existence. Robertson *et al.* (2010) and Taylor and Robertson (2011) developed a computational approach that combines the discrete vortex method and lubrication theory to calculate the evolution and growth of rivulets on a cable surface under combined effects of pressure, shear, surface tension, and gravity. They further investigated the effects of the initial water film thickness and the attacking angle on the development of rivulets with this numerical model (Taylor and Robertson 2015). Bi *et al.* (2013) derived two-dimensional (2-D) coupled equations of water film evolution by combining lubrication and single-mode system vibration theories. The water film evolution was numerically investigated by solving the coupled equations. Cheng *et al.* (2015) combined the direct numerical simulations and large eddy simulations to simulate the entire formation process of the water rivulets and categorized the rainwater morphology into four types of pattern during the analysis of the entire evolution process: collision–splashing, accumulation–slipping, formation–breaking, and dynamic equilibrium.

Nevertheless, experimental studies on the rivulet are very limited because the rivulet is considerably small, thin, and sensitive to wind flow. Directly measuring rivulets on site or in a wind tunnel is difficult. To the best knowledge of the authors, only few experiments have been carried out in literature. Cosentino *et al.* (2003) measured the thickness and movement of the upper rivulet using eight pairs of wires. Li *et al.* (2010a) and Chen *et al.* (2013) employed an ultrasonic technique to measure the shape, thickness, position, and movement of the rivulets on an inclined stay cable model in a wind tunnel test. Recently, Hu *et al.* (2015) developed a digital fringe projection system to measure the thickness distribution of wind-driven water droplet/rivulet flowing over a test plate. This system was feasible and of high resolution for rivulet thickness measurement. Li *et al.* (2015) proposed a videogrammetric technique to measure the rivulet movement along the entire cable during RWIV. However, the wires in Cosentino *et al.* (2003) had disturbance on the formation of rivulet and wind flow. Li *et al.* (2010a) measured the rivulet at specific sections of the cable, and the rivulet distribution on the cable was not available. The digital fringe projection system proposed by Hu *et al.* (2015) is complicated, expensive, and not applicable to vibration test.

In the present study, the videogrammetric technique adopted by Li *et al.* (2015) is extended so that it can synchronously measure the movement and thickness of the rivulet along the entire cable during RWIV in a wind tunnel. The technique is non-destructive, cost effective, and offers multi-point measurement and high resolution. For these, it has been applied to measure bridge displacement (Ye *et al.* 2013, 2015, Lee and Shinozuka 2006), Kalman vortex street (Pankanin *et al.* 2007), and cable vibration (Zhou *et al.* 2012).

The paper is organized as follows. Section 2 introduces the wind tunnel test set-up and experiment process. Section 3 describes the videogrammetric technique and the associated video processing, including the cable displacement measurement, rivulet position, and thickness identification. Sections 4 and 5 respectively show the identified rivulet position and thickness, as

well as the relationships among rivulet oscillation, thickness, and cable vibration. Conclusions are drawn in Section 6.

2. Wind tunnel test

This wind tunnel test was conducted in an open-jet wind tunnel. The rectangular outlet section measures 1.34 m wide and 1.54 m high. The cable model has an inclined angle $\alpha = 32°$ and a yaw angle $\beta = 35°$ (Fig. 1), resulting in the relative yaw angle $\beta^* = \sin^{-1}(\sin\beta\cos\alpha) = 29.1°$. The model was suspended by four springs at both ends in the vertical plane and supported by a steel wire in the longitudinal direction. The springs were mounted normal to the cable axis on a firm steel frame (not shown in Fig. 1). The cable model is 160 mm in diameter and 2.7 m in length, with a 2 m-long test segment in the middle and transition segments at both ends. It is made of a steel tube coated by polyethylene, the same as real stay cables. The mass of the entire cable model was measured as 66.0 kg. The fundamental frequency was identified as 1.39 Hz in free vibration tests, and the damping ratio was 0.05%. The corresponding Scruton number was calculated as $S_c = 4\pi m\xi / \rho D^2 = 6.72$, where ξ is the damping ratio, ρ is the air density, m is the mass of the cable model per unit length, and D is the cable diameter. RWIV of the cable model was tested under two wind speeds of 12.1 m/s and 14.1 m/s, corresponding to the Reynolds number ($R_e = UD/v$, where U denotes the wind speed and v denotes the kinematic viscosity) of 1.3×10^5 and 1.5×10^5, respectively. Both are consistent with the typical RWIV conditions observed by other researchers, for example, Hikami and Shiraishi (1988), Cosentino *et al.* (2003), and Gu and Du (2005).
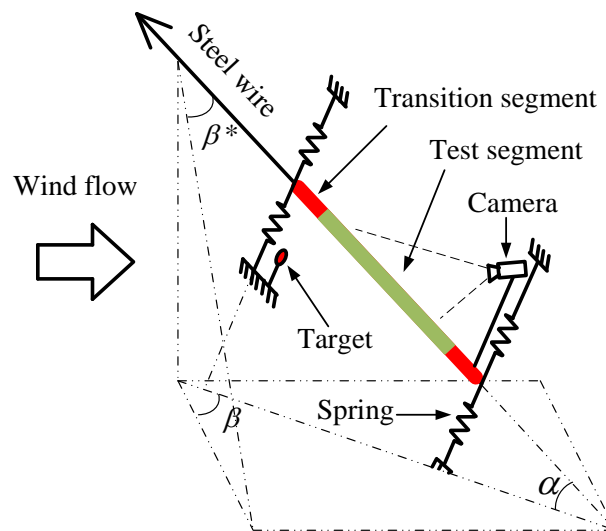

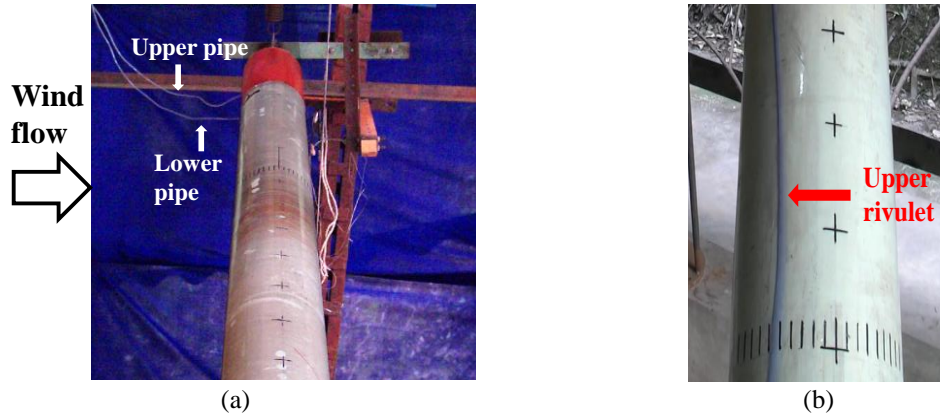Fig. 1 Setup of the cable experiment

Fig. 2 Simulation of upper and lower water rivulets

A digital video camera was mounted 1.2 m above the bottom end of the cable (Fig. 1) to ensure that the rivulet and wake flow were not disturbed. The camera moved with the cable and recorded the rivulet during RWIV. It captured 25 frames per second, each has the resolution of 720 (height) × 1280 (width) pixels. The movement and thickness of rivulet were then obtained by using the image processing method, which is introduced in detail in the next section. Moreover, a target with a ruler was fixed at the suspending frame so the camera could simultaneously measure the relative movement between the target and the camera. Given that the target was stationary and the camera moved with the cable, the measured relative movement was actually the camera movement and the cable displacement. The ruler was installed parallel to the direction of the cable vibration.

Images in the video clip are very sensitive to lighting. The same color under different lighting displays differently in digital images. Therefore, the lighting system has been carefully adjusted to conduct the tests under uniform lighting condition.

Two water rivulets guided by two flexible plastic pipes at the top end of the test segment (Fig. 2) simulate the upper and lower water rivulets. The rivulets flow from the top end to the bottom by the action of gravity, inertia, and wind pressure. This rivulet simulation has been verified to be effective as spraying water on the cable surface in reproducing RWIV in a wind tunnel (Li *et al.* 2015, Jing *et al.* 2015). Fig. 2(b) shows an upper water rivulet simulated with the present method.

3. Video processing

The video clips are processed to identify cable displacement, rivulet position, and rivulet thickness.

3.1 Identification of cable displacement in video

As described previous, the cable displacement is actually the camera displacement or the relative motion of the stationary target in video clips. The cable displacement is then identified using a simple image processing technique, which includes the following steps:

1. Transfer the video clip into a series of still images.

2. Identify the locations of the target and the ruler in the image when the cable is static. This image is referred to as the "reference image" [see Fig. 3(a)].

3. Identify the location of the cross-shaped target in the image when the cable vibrates (Zhou *et al.* 2012).

4. Transfer the location of the target in each image into the physical location. The position of the target in the *k*-th image is compared with that in the reference image. The difference in position denotes the cable displacement. For example, as shown in Figs. 3(b) and 3(c), y_k and y_{k+1} represent the displacement of the cable at the *k*-th and (*k*+1)-th instants respectively. The scale of the reference rule is calibrated before the tests. The downward movement is set as positive for the cable displacement.

3.2 Identification of rivulet position

The rivulet position is identified via three steps: image pre-processing, rivulet identification, and rivulet locating (Li *et al.* 2015).

3.2.1 Image pre-processing

Similar to the process in Section 3.1, the video clip is first converted into a series of RGB images (Fig. 4). Each RGB image is digitized into a three-dimensional matrix with the size of 720×1280×3, which represents the RGB intensity of each pixel. To reduce the computational loading, the irrelevant region in the RGB images is cropped, such that only the area comprising the cable and rivulet (i.e., the computational region) remains. The cropped images are adjusted using the histogram equalization method (Wang *et al.* 1999) to enhance the contrast and make the rivulet more distinguishable. The cropped and enhanced RGB images are converted into a grayscale image (Fig. 5). The grayscale image is expressed as a 2-D matrix A_0^k with the size of 200 (row) × 750 (column), where *k* denotes the *k*-th image. Each item in the matrix represents the gray intensity of the pixel. Black has the weakest intensity (0), whereas white has the strongest (255). The rivulet appears darker than the surrounding white cable surface because the water rivulet is colored in blue. Consequently, the intensity of the rivulet is weaker, and the corresponding items in the matrixes A_0^k are smaller than the others.

3.2.2 Identifying rivulet in the image

During the experiment the lighting condition may vary slightly over time, causing the background of each image is slightly different. The background of each image is thus removed by deducting the averaged value of the adjacent 21 images, corresponding to one cycle of rivulet vibration.

$$A^k = A_0^k - avg(A_0^{k-10}, \cdots, A_0^{k+10})$$

(1)

where A^k and A_0^k respectively denote the intensity matrixes after and before removing the background of the *k*-th image. The intensity values in A^k where the rivulet is located are smaller than the intensity value at other positions. Fig. 6 shows the intensity values of one column in A^k and A^{k-1}. The rivulet position in A^k has the minimum intensity, so does A^{k-1}. It also denotes that the rivulet positions in the two images are different because of the movement of the rivulet. In this

regard, the intensity difference $\Delta A^k = A^k - A^{k-1}$ is also shown in the figure and the rivulet position has the maximum intensity difference.

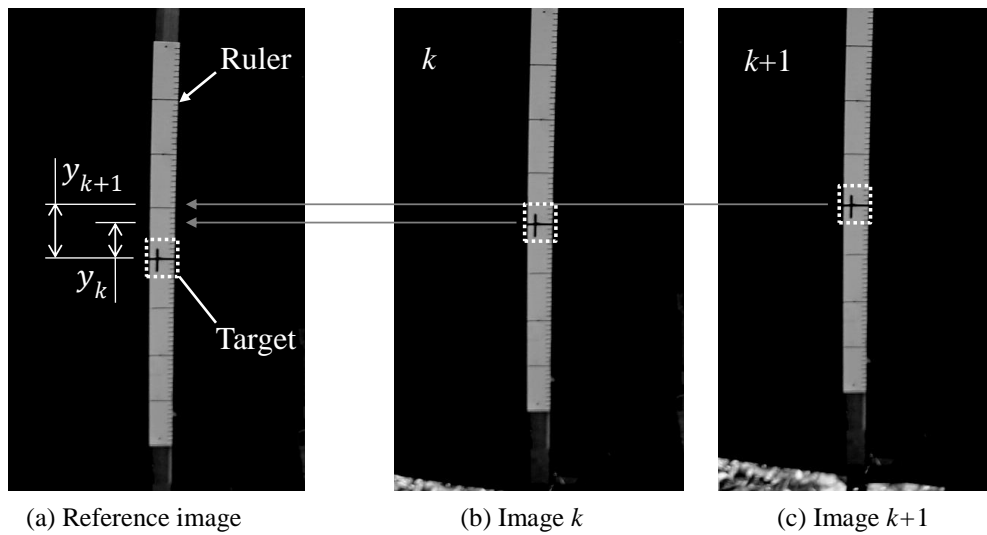| (a) Reference image | (b) Image k | (c) Image $k+1$ |

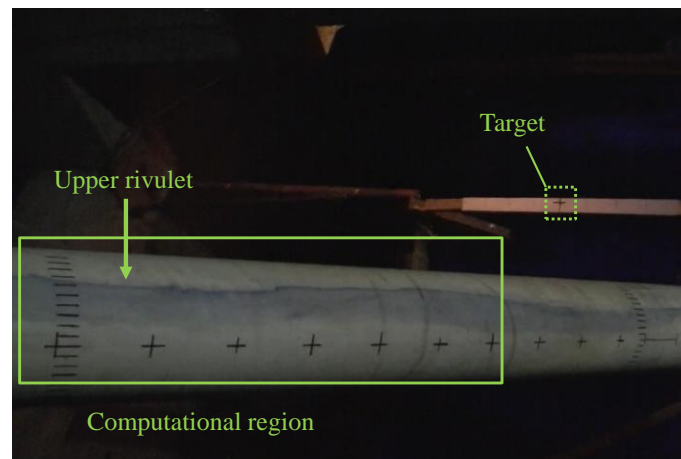Fig. 3 Identification of cable displacement
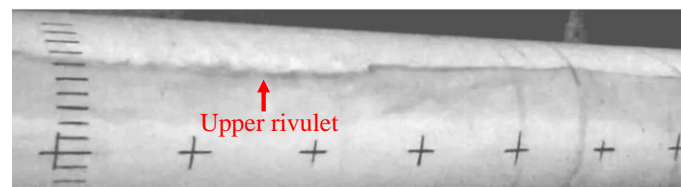

Fig. 4 An original image from the video clip

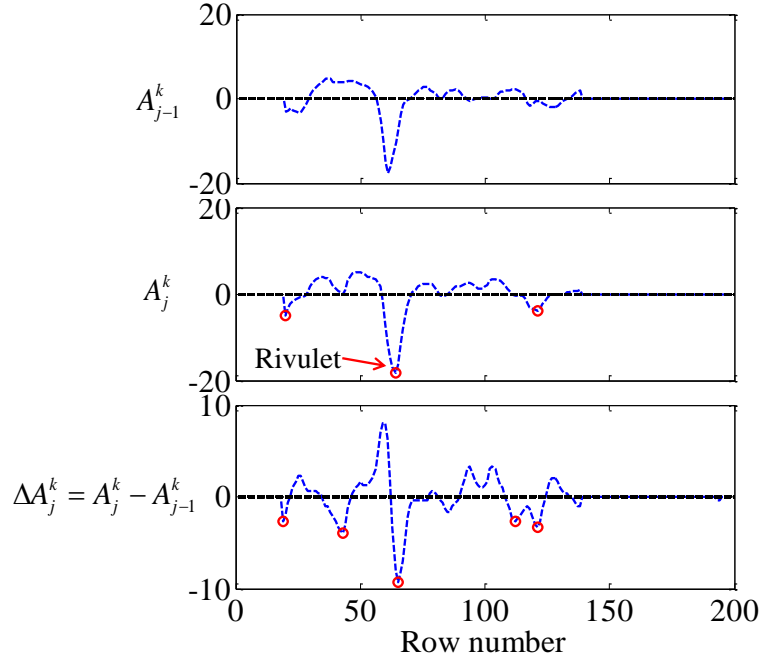Fig. 5 Cropped and enhanced grayscale image

Fig. 6 An example of rivulet identification

According to the above observation, the rivulet location can be identified by the following two features under ideal conditions: 1) the rivulet position has the minimal intensity in matrix A^k, and 2) the rivulet position has the maximal difference between A^k and A^{k-1}.

Here, the two approaches are integrated as follows:

(1) Calculate the intensity change as $\Delta A^k = A^k - A^{k-1}$.

(2) For each column j, the intensity is A_j^k and intensity change is ΔA_j^k.

(3) Obtain the local minimums of A_j^k.

(4) If the local minimum has a large reduction from the previous image, then the point is determined as the rivulet and the row number is the position of the rivulet.

(5) Otherwise, the global minimum of A_j^k is determined as the rivulet.

(6) Let $j=j+1$ until all columns are identified. The rivulet location at j-column of the k-th image is denoted as $RL(k, j)$.

In Fig. 6, the global minimum of A_j^k is determined as the rivulet location, which shows the largest reduction from the previous image (global minimum of ΔA^k) and coincides with one of the local minimums of A_j^k.

3.2.3 Locating rivulets on the cable surface

$RL(k, j)$ is the rivulet position in the image, which is then converted to the physical position on the cable surface. A virtual grid is established in the grayscale image based on the marks on the

cable surface [Fig. 7(a)]. The distance of the grids on the cable surface is 1 cm in the circumferential direction and 10 cm in the longitudinal direction. The rivulet position on the cable surface is calculated through linear interpolation of the grids because the virtual grid is equivalent to the cable surface in the image. Consequently, the location of the rivulet on the cable surface is obtained in terms of the longitudinal distance to the origin and circumferential angle θ. As shown in Fig. 7(b), θ measures from the top of the cable, and is positive in the anti-clockwise direction. Only the wind normal to the cable axis is illustrated in the figure. The angle between the horizontal and wind directions, ϕ, is expressed as Eq. (2) (Wilde and Witkowski 2003) and calculated as 20.4°.

$$\phi = \arcsin\left(\frac{\sin \alpha \sin \beta}{\sqrt{\cos^2 \beta + \sin^2 \alpha \sin^2 \beta}}\right) \tag{2}$$

The spatial resolution of the camera on the cable surface was about 1.2 mm/pixel, resulting in an angle resolution in the circumferential direction of 0.8°/pixel approximately.

3.3 Rivulet thickness

The colored rivulet has a small intensity in A^k, and the greater the amount of water, the smaller the intensity. Thus, the relative intensity of the pixel is proportional to the water thickness (radial thickness) as follows

$$T = C \times H \tag{3}$$

(a) Virtual grid

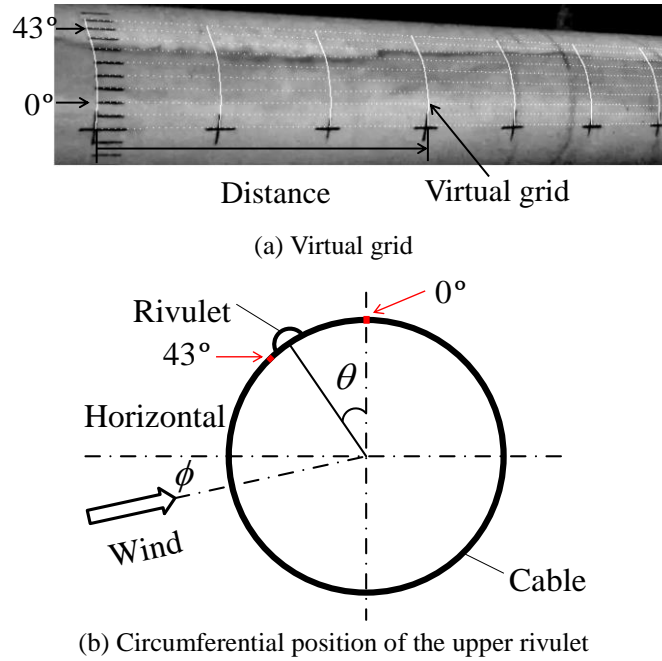(b) Circumferential position of the upper rivulet
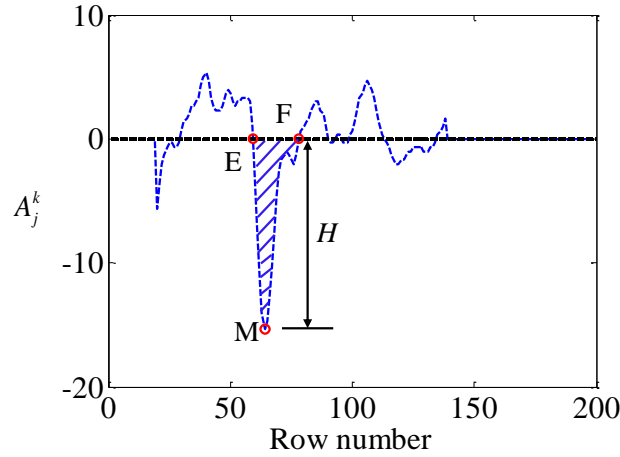
Fig. 7 Rivulet position on the cable surface

Fig. 8 Measurement of rivulet thickness

where T denotes the water thickness, C is the scale factor, and H is the absolute value of the relative intensity of the pixel, which can be obtained from Section 3.2. The pixel has the same intensity as the background when $H = 0$, indicating no rivulet. C is obtained by scaling the intensity, such that the cross-sectional area of the measured rivulet (S_m) equals that of the real rivulet (S), which is obtained from the water flow of the plastic pipe. That is

$$S = C \times S_m \tag{4}$$

Fig. 8 shows an example of the calculation of C. The rivulet location has been identified at point M, the point with the largest absolute value of relative intensity $H = 15$. EF is the rivulet width. The area surrounded by curve EMF, S_m, is the cross-sectional area of the measured rivulet and is calculated as 80.72 mm (relative intensity of pixels, H is dimensionless). The cross-sectional area of the real rivulet is equal to the water flow rate dividing by the flow speed, that is, $S = Q/V$, where Q is the water flow rate in the plastic pipe and is measured as 7.46×10^{-7} m^3/s, and V is the flow speed of the rivulet on the inclined cable, which is measured as 0.128 m/s. Therefore, S is calculated as 5.84 mm^2, and $C = 5.84/80.72 = 7.23 \times 10^{-2}$ mm. Consequently, the rivulet thickness is calculated using Eq. (3).

4. Characteristics of the upper rivulet oscillation

The large RWIV of the cable was successfully reproduced in the open-jet wind tunnel under the wind speed $U = 12.1$ m/s. The cable displacement and upper rivulet movement were identified from the same video clip using the image processing methods described in Sections 3.1 and 3.2. Fig. 9 illustrates the time history and power spectral density (PSD) of the cable displacement. The cable steadily vibrates at its fundamental frequency of 1.37 Hz with the amplitude of 66.3 mm.

The time-dependent spatial distribution of the upper rivulet position (θ) along the cable is shown in Fig. 10. The upper rivulet at the individual section of the cable periodically oscillates in

the circumferential direction. The oscillation feature at different sections along the cable axis is similar but not perfectly uniform. The oscillation amplitudes are different along the cable axis. Fig. 11 shows an example of the upper rivulet distribution at 15.44 s. The circumferential position of the upper rivulet at different cable sections is then averaged at each time instant.
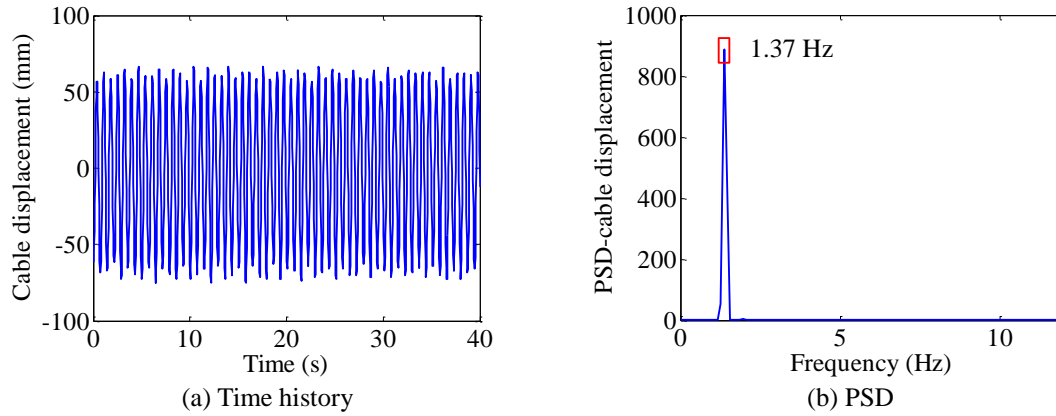

(a) Time history   (b) PSD

Fig. 9 Time history and PSD of cable displacement

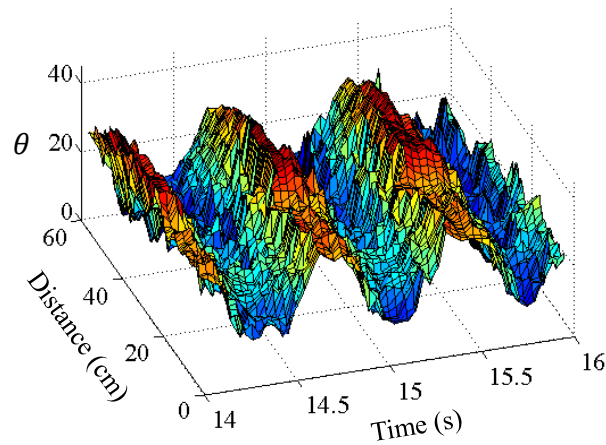Fig. 10 Time-dependent spatial distribution of the upper rivulet
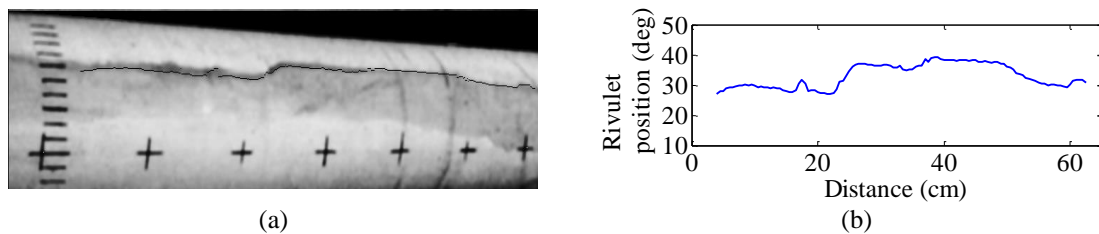

(a)   (b)

Fig. 11 Identified upper rivulet position along the cable at 15.44 s

(a) Time history of the upper rivulet position

(b) PSD of the upper rivulet position

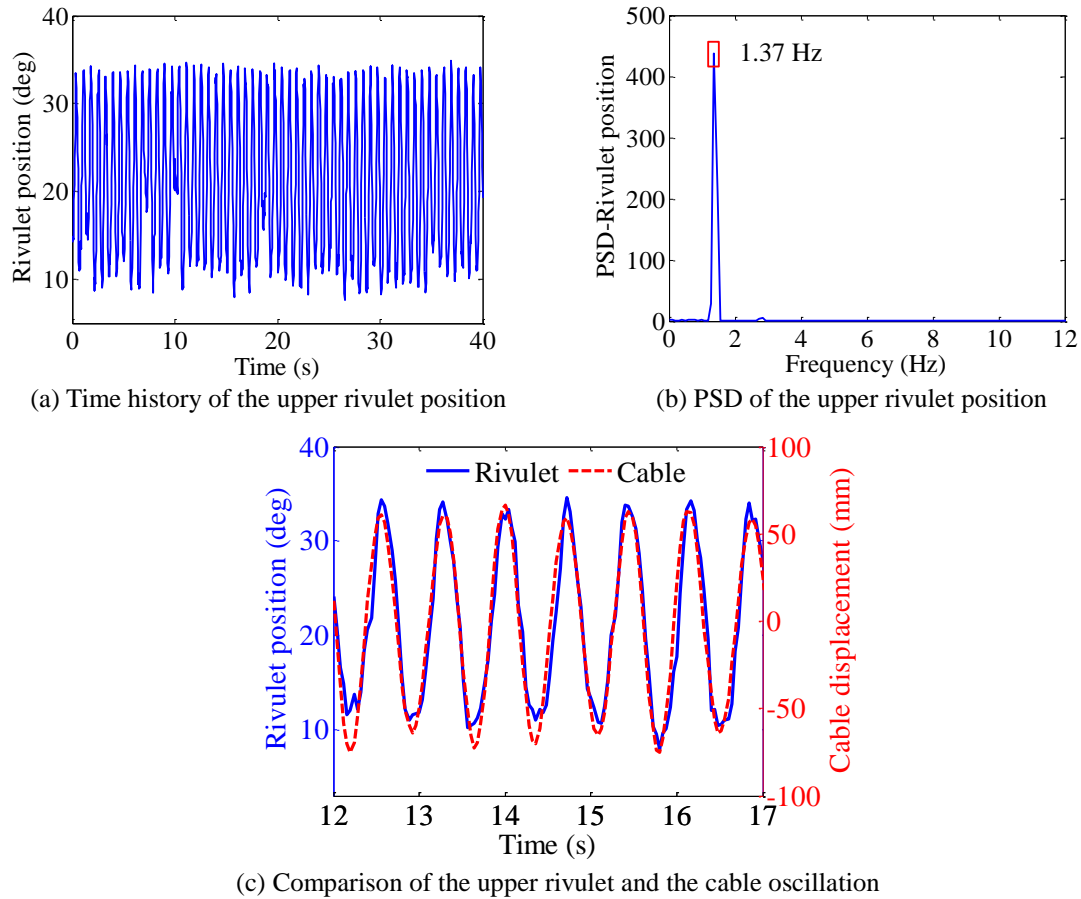(c) Comparison of the upper rivulet and the cable oscillation

Fig. 12 Upper rivulet position and cable displacement when $U = 12.1$ m/s

Figs. 12(a) and 12(b) show the time history and corresponding PSD of the averaged upper rivulet movement respectively. The averaged upper rivulet regularly oscillates between 8° and 34° with the equilibrium position at 21°. The dominant frequency is 1.37 Hz, which is comparable to the vibration frequency of the cable. These results coincide with those in previous studies. For example, Cosentino *et al.* (2003) observed the mean position of the upper rivulet oscillated between 13° and 25° with the equilibrium position 20° approximately under the wind speed of 9 m/s, $\alpha = 25°$, and $\beta = 30°$. Li *et al.* (2010a) measured the upper rivulet oscillated around the equilibrium position 35° with the root mean square of 7° at the cable fundamental frequency under the wind speed of 7.7 m/s, $\alpha = 30°$, and $\beta = 22.5°$. The differences in the equilibrium position and oscillation amplitude might be caused by the different inclination and yaw angles and different wind speed. Fig. 12(c) compares the averaged upper rivulet movement and the cable vibration. Both oscillations are steady, regular, and in-phase, similar to those obtained by Cosentino *et al.* (2003). Moreover, the averaged upper rivulet oscillates away from the cable top (i.e., from 8° to 34°) when the cable moves downward (i.e., from −64 mm to 68 mm). However, it oscillates

toward the cable top (i.e., from 34° to 8°) when the cable moves upward (i.e., from 68 mm to –64 mm).

Similar results have been observed under the wind speed of U = 14.1 m/s. The cable vibrates at the fundamental frequency with the amplitude of 40.2 mm. The upper rivulet steadily, regularly, and circumferentially oscillates on the cable surface. The oscillation feature is similar but not perfectly uniform along the cable axis. The averaged upper rivulet oscillates between 7° and 35° with the equilibrium position of 21° at the fundamental frequency of the cable. The averaged upper rivulet movement and the cable oscillation are in-phase.

5. Thickness of the upper rivulet during oscillation

The rivulet thickness along the entire cable is also identified from the video clip, as described in Section 3.3. Fig. 13 shows the thickness distribution of the identified upper rivulet along the cable axis at 15.44 and 15.84 s when the cable is at the lowest and highest positions respectively. The thickness distribution at 15.44 s is thicker than that at 15.84 s. The thickness varies along the cable axis and it is then averaged. Fig. 14 shows the time history and PSD of the averaged upper rivulet thickness. The upper rivulet thickness varies between 0.17 and 1.15 mm when the upper rivulet moves on the cable surface. The mean upper rivulet thickness is calculated as 0.45 mm. Similar results were also observed in previous wind tunnel tests. Cosentino *et al.* (2003) observed the upper rivulet thickness varied between 0.15 and 0.6 mm in wind tunnel tests. The computational fluid dynamics simulation by Taylor and Robertson (2015) showed that the upper rivulet varied between 0.25 to 0.35 mm through when the cable was static. Li *et al.* (2010a) measured the rivulet thickness at a certain section as 0.51 mm, which is close to the present mean rivulet thickness. Two dominant frequencies are observed in PSD, 1.37 and 2.83 Hz. The first dominant frequency coincides with the cable fundamental frequency and the second is roughly double the first while with smaller PSD amplitude.

The detailed time history of the averaged upper rivulet thickness is shown in Fig. 15. The upper rivulet thickness periodically and alternately changes. The duration of the thick upper rivulet within one period is about half of that of the thin rivulet. The rivulet thickens when it moves away from the cable top (i.e., 10° to 34°) and reaches its thickest at the farthest position away from the top (i.e., approximately 34°). However, it becomes thin when it moves back close to the cable top. The thin upper rivulet lasts longer than the thick one. This character is confirmed by the locus in Fig. 15(b). The combination of the obtained relationship between the upper rivulet oscillation and the cable vibration reveals that the upper rivulet thickens when the cable reaches the lowest position, whereas it becomes thin when the cable moves back to the highest position.
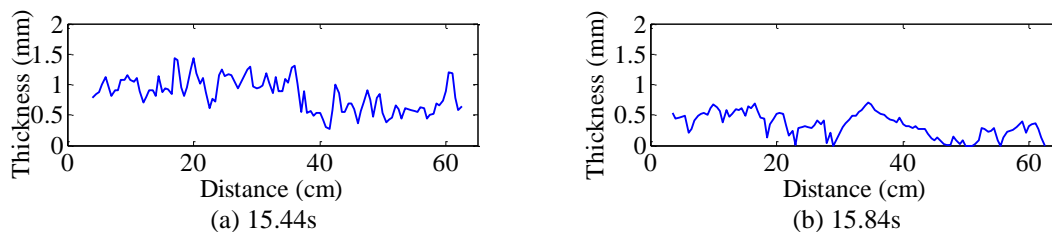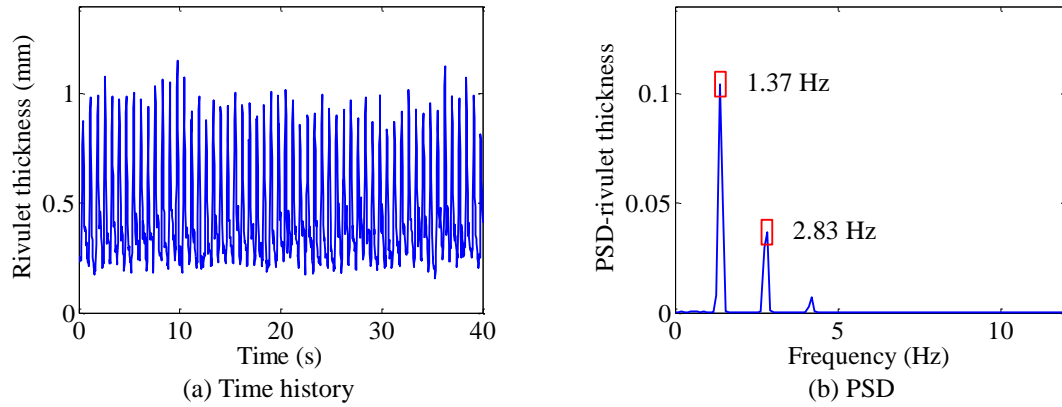

Fig. 13 Rivulet thickness along the cable

Fig. 14 Time history and PSD of the upper rivulet thickness when $U = 12.1$ m/s
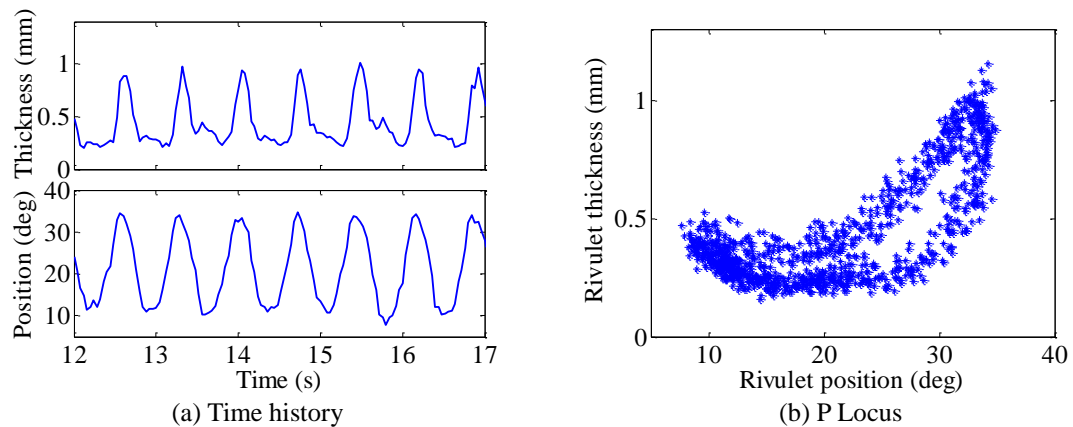

Fig. 15 Comparison of thickness and position of the upper rivulet ($U = 12.1$ m/s)

Similar results are observed from Fig. 16, when wind speed $U = 14.1$ m/s. The upper rivulet thickness varies between 0.05 and 1.08 mm with the temporal average of 0.38 mm. Compared with the case of $U = 12.1$ m/s, the main features of these two cases are similar. The rivulet thickness periodically varies at the dominant frequencies of 1.37 and 2.83 Hz. The duration of the thick rivulet within a single period is also shorter than that of the thin rivulet. The upper rivulet becomes thicker when it moves away from the cable top and the cable vibrates to the lowest position. However, the upper rivulet becomes thinner when the upper rivulet and the cable oscillate in the opposite direction. Their difference is that the upper rivulet under $U = 14.1$ m/s is thinner than that of $U = 12.1$ m/s, and the former varies less regularly and steadily than the latter.
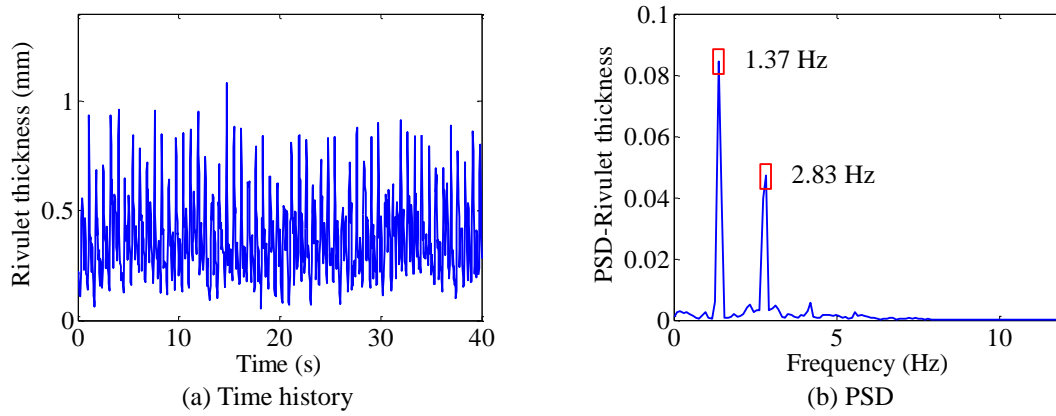
Fig. 16 Time history and PSD of the upper rivulet thickness when $U = 14.1$ m/s

The difference might be attributed to the different cable vibration amplitudes and wind speeds. Cosentino *et al.* (2003) and Jing *et al.* (2015) reported that the variations of the upper rivulet position and thickness are related to the wind speed and cable vibration. The upper rivulet has been widely reported being located close to the separation point of the inclined cable. The flow separation point and state of the inclined cylinder changes with the R_e. Therefore, R_e and the corresponding wind speed should significantly affect the thickness and movement of the upper rivulet. Moreover, the initial force from the cable vibration is one of the main excitations of the upper rivulet. The cable vibration should also affect the movement and thickness of the upper rivulet.

6. Conclusions

In this study, the large-amplitude RWIV of a cable model was reproduced in an open-jet wind tunnel. The cable displacement, upper rivulet position, and thickness were simultaneously measured using the videogrammetric technique. The characteristics of the upper rivulet movement and thickness were obtained along the entire cable. The position and thickness of the upper rivulet vary with the cable vibration. The relationships among upper rivulet oscillation and thickness, as well as cable vibration were obtained. The following conclusions can be drawn from the experiment:

1) The proposed non-contact videogrammetry method to measure the rivulet position and thickness along the whole cable is efficient and cost effective.

2) The upper rivulet oscillates circumferentially on the cable surface at the same frequency of the cable when a large RWIV of the cable occurs. The oscillation features of different sections along the cable axis are similar.

3) The averaged upper rivulet position oscillates in-phase with the cable vibration when a large RWIV occurs.

4) The thickness of the upper rivulet periodically varies when the rivulet oscillates on the cable

surface. The upper rivulet becomes thickest when it reaches the farthest position from the cable top and the cable simultaneously arrives at the lowest position.

Acknowledgements

References

Bi, J.H., Wang, J., Shao, Q., Lu, P., Guan, J. and Li, Q.B. (2013), "2D numerical analysis on evolution of water film and cable vibration response subject to wind and rain", *J. Wind Eng. Ind. Aerod.*, **121,** 49-59.

Chen, W.L., Tang, S.R., Li, H. and Hu, H. (2013), "Influence of dynamic properties and position of rivulet on rain-wind-induced vibration of stay cables", *J. Bridge Eng.*, **18**(10), 1021-1031.

Cheng, P., Li, H., Fuster, D., Chen, W.L. and Zaleski, S. (2015), "Multi-scale simulation of rainwater morphology evolution on a cylinder subjected to wind", *Comput. Fluid*, **123**, 112-121.

Cosentino, N., Flamand, O. and Ceccoli, C. (2003), "Rain-wind induced vibration of inclined stay cables, Part I: experimental investigation and physical explanation", *Wind Struct.*, **6**(6), 471-484.

Gu, M. and Du, X.Q. (2005), "Experimental investigation of rain-wind-induced vibration of cables in cable-stayed bridges and its mitigation", *J. Wind Eng. Ind. Aerod.*, **93**, 79-95.

Hikami, Y. and Shiraishi, N. (1988), "Rain-wind induced vibrations of cables stayed bridges", *J. Wind Eng. Ind. Aerod.*, **29**, 408-418.

Hu, H., Wang, B., Zhang, K., Lohry, W. and Zhang, S. (2015), "Quantification of transient behavior of wind-driven surface droplet/rivulet flows using a digital fringe projection technique", *J. Visualization*, **18**, 705-718.

Jing, H.Q., Xia, Y., Li, H., Xu, Y.L. and Li, Y.L. (2015), "Study on the role of rivulets in rain-wind induced cable vibration through wind tunnel testing", *J. Fluid Struct.*, **59**, 316-327.

Lee, J.J. and Shinozuka, M. (2006), "Real-time displacement measurement of a flexible bridge using digital image processing techniques", *Exp. Mech.*, **46**, 105-114.

Lemaitre, C., de Langre, E. and Hémon, P. (2010), "Rainwater rivulets running on a stay cable subject to wind", *Eur. J. Mech. B*, **29**(4), 251-258.

Lemaitre, C., Hémon, P. and de Langre, E. (2007), "Thin water film around a cable subject to wind", *J. Wind Eng. Ind. Aerod.*, **95**, 1259-1271.

Li, F.C., Chen, W.L., Li, H. and Zhang, R. (2010a), "An ultrasonic transmission thickness measurement system for study of water rivulets characteristics of stay cables suffering from wind-rain-induced vibration", *Sens. Actuators A*, **159**(1), 12-23.

Li, H., Chen, W.L., Xu, F., Li, F.C. and Ou, J.P. (2010b), "A numerical and experimental hybrid approach for the investigation of aerodynamic forces on stay cables suffering from RWIV", *J. Fluid Struct.*, **26**(7-8), 1195-1215.

Li, Y.L., Jing H.Q., Xia Y., Xu Y.L. and Xiang H.Y. (2015), "Measurement of rivulet movement on inclined cables during rain-wind induced vibration", *Sens. Actuat. A*, **230**, 17-24.

Main, J.A. and Jones, N.P. (1999), "Full-scale measurements of stay cable vibration", *Wind Engineering into the 21st Century*, A. A. Balkema, Rotterdam, 963-970.

Matsumoto, M., Saitoh, T., Kitazawa, M., Shirato, H. and Nishizaki, T. (1995), "Response characteristics of

rain-wind Induced vibrations of stay-cables of cable-stayed bridges", *J. Wind Eng. Ind. Aerod.*, **57**, 323-333.

Matsumoto, M., Shiraishi, N. and Shirato, H. (1992), "Rain-wind induced vibration of cables of cable-stayed bridges", *J. Wind Eng. Ind. Aerod.*, **43**, 2011-2022.

Matsumoto, M., Yagi, T., Goto, M. and Sakai, S. (2003), "Rain-wind-induced vibration of inclined cables at limited high reduced wind velocity region", *J. Wind Eng. Ind. Aerod.*, **91**, 1-12.

Matsumoto, M., Yokoyama, K., Miyata, T., Fujino, Y. and Yamaguchi, H. (1989), "Wind- induced cable vibration of cable-stayed bridges in Japan", *Proceedings of the Canada-Japan Workshop on Bridge Aerodynamics*, 101-110.

Ni, Y.Q., Wang, X.Y., Chen, Z.Q. and Ko, J.M. (2007). "Field observations of rain-wind induced cable vibration in cable-stayed Dongting Lake Bridge", *J. Wind Eng. Ind. Aerod.*, **95**, 303-328.

Ohshima, K. and Nanjo, M. (1987), "Aerodynamic stability of the cables of a cable-stayed bridge subject to rain (a case study of the Ajigawa Bridge)", *Proceedings of the 3rd US-Japan Bridge Workshop*, Tsukuba, Japan.

Pankanin, G.L., Kulinczak, A. and Berlinski, J. (2007), "Investigations of Karman vortex street using flow visualization and image processing", *Sens. Actuat. A*, **138**, 366-375.

Robertson, A.C., Taylor, I.J., Wilson, S.K., Duffy, B.R. and Sullivan, J.M. (2010), "Numerical simulation of rivulet evolution on a horizontal cable subject to an external aerodynamic field", *J. Fluid Struct.*, **26**(1), 50-73.

Saito, T., Matsumoto, M. and Kitazawa, M. (1994), "Rain-wind excitation of cables on cable-stayed Higashi-Kobe Bridge and cable vibration control", *Proceedings of Conference on Cable-Stayed and Suspension Bridges*.

Seidel, C. and Dinkler, D. (2006), "Rain-wind induced vibrations-phenomenology, mechanical modeling and numerical analysis", *Comput. Struct.*, **84**(24-25), 1584-1595.

Taylor, I.J. and Robertson, A.C. (2011), "Numerical simulation of the airflow- rivulet interaction associated with the rain-wind induced vibration phenomenon", *J. Wind Eng. Ind. Aerod.*, **99**, 931-944.

Taylor, I.J. and Robertson, A.C. (2015), "Numerical investigation of the coupled interaction between an unsteady aerodynamic flow field and a water film coating on a circular cylinder", *J. Fluid Struct.*, **54**, 312-331.

Wang, L.Y. and Xu, L.Y. (2003), "Analytical study of wind-rain-induced cable vibration: 2DOF model", *Wind Struct.*, **6**(4), 291-306.

Wang, Y., Chen, Q. and Zhang, B.M. (1999), "Image enhancement based on equal area dualistic sub-image histogram equalization method", *IEEE Trans. Consum. Electron.*, **45**, 68-75.

Wilde, K. and Witkowski, W. (2003), "Simple model of rain–wind-induced vibrations of stayed cables", *J. Wind Eng. Ind. Aerod.*, **91**, 873-891.

Xia, Y. and Fujino, Y. (2006), "Auto-parametric vibration of a cable-stayed-beam structure under random excitation", *J. Eng. Mech.- ASCE*, **132**(3), 279-286.

Xu, Y.L. and Wang, L.Y. (2003). "Analytical study of wind-rain-induced cable vibration: SDOF model", *J. Wind Eng. Ind. Aerod.*, **91**, 27-40.

Ye, X.W., Ni, Y.Q., Wai, T.T., Wong, K.Y., Zhang, X.M. and Xu, F. (2013), "A vision-based system for dynamic displacement measurement of long-span bridges: algorithm and verification", *Smart Struct. Syst.*, **12**(3-4), 363-379.

Ye, X.W., Yi, T.H., Dong, C.Z., Liu, T. and Bai, H. (2015), "Multi-point displacement monitoring of bridges using a vision-based approach", *Wind Struct.*, **20**(2), 315-326.

Zhou, X.Q., Xia, Y., Wei, Z.L. and Wu, Q.X. (2012). "A videogrammetric technique for measuring the vibration displacement of stay cables", *Geo-spatial Inform. Sci.*, **15**, 135-141.

Zuo, D.L., Jones, N.P. and Main, J.A. (2008). "Field observation of vortex- and rain-wind-induced stay-cable vibrations in a three-dimensional environment", *J. Wind Eng. Ind. Aerod.*, **96**, 1124-1133.